Failure Modelling and Characterisation for Pin-Reinforced Metal-Composite Joints

Alex T.T. Nguyen[1,2], Natdanai Pichitdej[2], Milan Brandt[2], Stefanie Feih[3,4] and Adrian C. Orifici[3♣]

[1] Engineering Mechanic Group, Institute of High Performance Computing, 1 Fusionopolis Way, Singapore 138632

[2] Additive Manufacturing Research Centre, School of Engineering, RMIT University, Melbourne, Australia

[3] Sir Lawrence Wackett Aerospace Research Centre, School of Engineering, RMIT University, Melbourne, Australia

[4] Joining Technology Group, Singapore Institute of Manufacturing Technology, 2 Fusionopolis Way, Singapore 138634

Published in: Composite Structures, 188 (2018) 185–196

♣ Corresponding author: adrian.orifici@rmit.edu.au

ABSTRACT

Through-thickness metallic pin reinforcements can significantly improve the performance of hybrid metal-composite joints, particularly when failing in the high-energy mode of pin pull-out. However, there is a lack of knowledge on how to promote pull-out across the wide range of joint parameters including geometry and load conditions. Here, a numerical methodology capturing all relevant pin geometry, material and damage characteristics is proposed, and shown to closely match experimental results. This model was then used to characterise pin failure mode and energy as a function of pin geometry across loading ratios ranging from pure tensile to pure shear. The numerical model provides extensive insight into the damage sequence and the interaction of damage mechanisms. The investigation also comprehensively reveals how increasing the shear loading component reduces the pin aspect ratio of height-to-diameter required to maintain pin pull-out. The results add new knowledge and capability for the optimum design of pin-reinforced hybrid joints.

1. INTRODUCTION

Hybrid metal-composite joints are increasingly explored for lightweight engineering applications due to the expanding use of carbon and glass fibre reinforced polymer composites (FRPs). New manufacturing technologies are available to enhance the fracture toughness of hybrid adhesive joint designs with the addition of through-thickness reinforcement pins. These pins are generally made out of metallic material and can be built directly onto the metallic adherend substrate using layer Additive Manufacturing (AM) (1) and Electron Beam surface texturing (2) or as separated entities and connected by Cold-Metal-Transfer (3), laser-cut metal sheets (4) and laser riveting through Selective Sintering Technique (5-7). Pin-reinforced hybrid joints exhibit remarkable energy absorption as the pins provide mechanical interlocking effects between the adherends. Previous publications (8, 9) by the authors characterised the response of single pin-reinforced hybrid joints focusing on pin interface properties with respect to pin length-to-diameter (*L/D)* aspect ratio, pin support conditions and mode mixity loading ratio. However, the pin pull-out behaviour was not characterized under the full range of mode mixity loading ratios. Furthermore, it is speculated that the pin critical *L/D* aspect ratio to achieve pin pull-out failure mode is affected by the mode mixity ratio as pin plastic deformation post pull-out was observed to increase with increasing values (9). Experimental studies for this process are expensive in terms of time and costs.

Numerical models capable of fully predicting the adhesion response of pin-reinforced hybrid joints currently do not exist due to the complex damage mechanisms, highly nonlinear behaviour of the joint and constantly changing boundary conditions. Each of these aspects requires highly detailed meshing and respectively large computational resources for analysis, especially at a structural level. Related numerical research on CFRP z-pin reinforced composites (10-14) showed that multi-scale analysis approaches are capable of predicting the properties of large scale structures efficiently. In this case, a high fidelity single pin model is developed to capture all damage modes and the respective pull-out load versus opening displacement relationship, which is usually referred to as the bridging law. This bridging law is subsequently incorporated into a less computationally intensive model at a structural level through the use of simple representative spring elements. The accuracy of this multi-scale approach depends on the capabilities of the single pin model. The precision of the single pin model lies in the ability to capture all possible damage mechanisms of pin failure, pin pull-out, resin matrix crushing, and composite ply fracture. Several numerical models have been developed to capture these phenomena separately, and each response is modelled with different techniques.

Bianchi et al. (10, 11), Meo et al. (15) and Li et al. (16) uses Coulumb friction/pressure contact interaction to model the interface behaviour between the pin and the composite. An external pressure or residual thermal stress from curing is typically applied on the structure with friction coefficient μ varied from 0.4 to 0.75. The pull-out load versus displacement response was shown to correlate well with experimental data. However, the microstructure of the composites such as fibre waviness, resin-rich zone and pin misalignment angle (17) was not taken in account, and no material damage was incorporated. Another method using cohesive elements to simulate the pin/composite interface behaviour was developed by Zhang et al. (12) and Cui et al. (13, 14). The pin/composite interface cohesive properties are typically calibrated with experimental data, and pin damage is simulated by further embedding different sets of cohesive elements to capture pin fracture. The results were shown to accurately capture the pin pull-out behaviour under mixed mode loading condition in terms of load versus displacement response and damage mechanisms. However, these models are highly mesh-dependent due to the manually inserted crack paths at the interface, and the calibrated interface cohesive parameters must be calibrated for different structures. All of the above models provide a good indication of the required modelling techniques to capture the pull-out response of the single pin. However, further work is required for metallic pin reinforced hybrid joints due to the fundamental differences in pin material, thermal coefficient of expansion, interface properties, and micro-structure of the joint.

In this work, a high fidelity single pin hybrid joint model based on the detailed microstructure of a hybrid Ti64-carbon fibre composite (CFRP) joint is generated. The titanium adherend including its surface pins was additively manufactured via selective laser melting (SLM). This approach allows for full control over pin geometry and density. Modelling parameters such as specimen definition, meshing scheme, boundary conditions, damage models and interface properties are presented in detail. Previously characterised interface properties of the 0° pin (small pin (D=0.5 mm, L=2.0 mm) and large pin (D=1.0 mm, L=3.5 mm)) and 20° offset angle pin (large pin (D=1.0 mm, L=3.5 mm)) are used for the calibration of interface parameters, load response and damage profile. The validated model is extended to investigate the pin pull-out behaviour of large pin (D=1.0 mm) specimens with varying length from 1.0 mm to 6.5 mm at an increment size of 0.5 mm under the full range of mode mix loading ratios. The results are used to map the relationship between *L/D* aspect ratio and mode mix ratio in terms of pin failure mode to define the critical transition aspect ratio $(L/D)_{crit}$ for all loading conditions. This design map is considered a major advancement in the development of pin-reinforced hybrid joints. Furthermore, together with the models at structural scale level and the multi-scale modelling methodology developed in previous publications, this high precision numerical model completes the numerical procedure needed for analysis and optimization of a pin-reinforced hybrid joint.

2. MODELLING METHODOLOGY

2.1. Specimen definition

The specimen definition used in this work is taken directly from the single pin experimental studies conducted in previous publications (8, 9) to characterise the pull-out performance and mode mix response of a single pin specimen. Essentially, one single Ti-6Al-4V pin reinforcing the hybrid CFRP composite-metallic joint was loaded in tension (pull-out) with variation in pin length (*L*) to diameter (D) aspect ratio and offset angle (see Figure 1).

The pin and its substrate were jointly manufactured via SLM in a build chamber of 250 mm × 250 mm × 350 mm (SLM250HL, SLM Solutions, Germany). A porosity content of less than 0.3% was obtained during the printing process (3D X-ray Computer Tomography) with an average surface roughness (S_a) of 10 μm ± 3 μm (Alicona IF-EdgeMaster profilometer). Further details of manufacturing parameters can be found in previously published experimental work (8, 9, 18). The hybrid specimens were manufactured by manually pressing the unidirectional composite pre-preg tape layers of T700 carbon/epoxy plies (VTM264, Advanced Composites Group) on top of the metal substrate. The whole system was co-cured in an autoclave for 1 hour at 120°C and 620 kPa. A polytetrafluoroethylene (PTFE) insert of 0.1 mm thickness at the interface of the titanium adherend and the composite ensured that only the pin pull-out response was measured. Typical in-plane microstructure of the specimen is summarised in Figure 2 showing distortion in composite microstructure with local fibre waviness around the pin, fibre breakage and a resin rich region.

Two different pin diameters were investigated: small pin (D = 0.5 mm) and large pin (D = 1.0 mm). Due to an inherent dimensional defect of the SLM manufacturing process caused by the attachment of partially melted particles, the circular cross-section of the small pin (D = 0.5 mm) became elliptical with D_1 = 0.55 mm and D_2= 0.67 mm, while the large pin (D = 1.0 mm) was largely unaffected with an increase in diameter from D = 1.0 mm to D = 1.05 mm. The pin cross-sectional area and circumference from the ellipse of best fit was included in the modelling scheme. The analysis matrix is indicated in Table 1. Both 0° small (D = 0.5 mm) and large (D = 1.0 mm) pins with lengths of 2mm and 3.5mm, respectively, are used for the calibration of interface cohesive parameters. The pull-out traction loads versus displacement results are used to validate the interface cohesive law. In addition, the large (D = 1.0 mm) 20° offset angle pin is used to calibrate the contact friction coefficient in the presence of bearing pressure. Finally, both cohesive and friction interaction parameters are applied to analyse the effect of pin offset angle and to characterise the pull-out response under the full range of mode mix loading ratio for a range of pins geometries.

2.2. Meshing scheme and interface modelling

Figure 2 illustrates the simulated geometry. The in-plane dimensions of the FE model are 10 mm × 10 mm (similar to the single pin experimental specimen), and the model is comprised of the composite laminate, titanium substrate and pin. The cross-section of the composite laminate closely follows the specimen microstructure architecture consisting of a resin-rich zone and localised fibre waviness around the pin due to fibre displacement following the pin insertion process. The distance H_1 and H_2, and V_1 and V_2 are assumed to be the horizontal and vertical boundaries of the fibre waviness region (see Figure 2). The relationship between each microstructure parameter with respect to the pin diameter was characterised (see Table 2) and presented in details in previous publications (8, 9). A cubic function generates the geometry of the fibre waviness, which is proportional to the diameter of the pins. The waviness is also assumed to reduce linearly from a maximum around the pin to be perfectly smooth and without waviness at the vertical distance V_1 and V_2, and the resin rich region runs in the through-thickness direction of the specimen. The resin-rich zone is also assumed to include in-plane fibre breakage and through-thickness fibre crimp. Lastly, the pin is modelled according to the modified cross-section, and the pin fillet at the root to the titanium adherend is included to accurately capture the stress concentrations causing pin failure.

Figure 3 shows a typical in-plane mesh of the FE model and highlights the specimen microstructure and the composite fibre orientation around the pin. Figure 4 indicates the through-thickness direction mesh of a 20° offset angle pin showing the resin-rich region and pin fillet. The composite plies are meshed with continuum shell elements (SC8R), while resin-rich regions and the titanium material are meshed with solid elements (C3D6 & C3D8). Typical element lengths within the composite plies, resin-rich and titanium sections are 0.1 mm, 0.15 mm and 0.05 mm, respectively. The total height of the pin-reinforced model is equivalent to the embedded pin length. The through-thickness dimensions of all elements are kept at 0.05 mm. A mesh sensitivity study was conducted with 0.025 mm through-thickness element length, and the results in terms of stress, damage and load response remained unchanged. The top and bottom face of the specimens are coupled in all D.O.F with a reference node and are loaded using displacement control to mimic the experimental test control.

There are three individual material regions in this model comprising of CFRP composite, resin rich zone and the titanium pin and substrate. The nodal locations at the interface of each part are coincident and are connected by different types of contact and constraints. The faces of the CFRP composite and the resin rich zone are connected together with tied constraint in all degrees of freedom. The interface between the resin rich zone and the titanium pin has a cohesive contact interaction coupled with Coulomb friction/contact pressure relationship to represent the interface properties between the two parts as indicated in more detail in Figure 5.

The modelling methodology of the interface is indicated in Figure 5, showing a close-up view of a typical mesh in an exploded state at the interface region. The cohesive interaction law at the titanium/resin interface, shown as C_2 in Figure 5, captures the basic interface properties. Additionally, a global contact definition of Coulomb friction/pressure relationship, shown as F in Figure 5, is set between all parts to capture the bearing effect should the titanium pin come into physical contact with the remaining parts. The relation between friction coefficient and bearing effect is analysed and calibrated in Section 6.4. Furthermore, in this methodology, the resin-rich zone is made up of several smaller parts and each part is connected with a cohesive interaction definition using the properties of a typical epoxy resin (shown as C_1 in Figure 5). This was necessary to simulate the crushing and spalling of the resin during mode mixed loading. A half model is used for the analysis of all cases with symmetry in the y-axis. Other modelling methods, such as element deletion and internally-generated surfaces once the pin comes into contact and crushes the surrounding resin elements, were trialled; however, the results resulted in unrealistic and inaccurate representation of bearing and spalling effects.

2.3. Damage, contact and material properties

All numerical models were solved using Abaqus Explicit 6.14 with a time period of 0.05 s. Automatic mass scaling was used to scale the stable time increment of the model from typically 1×10^{-9} to 1×10^{-8} with minimal dynamic effects. For the pull-out analysis, the applied displacement is set to be equivalent to the length of the pin with a smooth step amplitude to promote quasi-static loading condition. The typical run time of each analysis on an Intel i7 4 core processor is 1.5 to 2.0 hours. The basic elastic properties for the CFRP, resin and titanium material are summarized in Table 3. In addition, non-linear damage models are implemented for resin and titanium using the Abaqus built-in ductile damage module. All contact definitions are defined using cohesive behaviour couple with frictional sliding. The details of damage models and contact definition are given in Section 2.3.1.

2.3.1. Titanium and resin ductile damage

To capture the pin plastic deformation and failure behaviour, the elastic-plastic material properties of SLM Ti-6Al-4V were applied with the Abaqus built-in ductile damage model (21). The power law fit shown in Equation 1 defines the plastic hardening behaviour:

$$\sigma_{pl} = 1070 + 575\varepsilon_{pl}^{0.44} \quad \text{Equation 1}$$

The onset of damage is determined by a metallic ductile criterion developed based on a phenomenological model of nucleation, growth, and coalescence of voids (22). In this criterion, the plastic strain (ε^{pl}) is defined as a function of stress triaxility (η) (see Equation 2), which is a dimensionless parameter defined by the ratio of hydrostatic pressure stress (p) (see Equation 3) and equivalent Mises stress (q) (see Equation 4)

$$\eta = -\frac{p}{q} \quad \text{Equation 2}$$

Where,

$$p = -\frac{1}{3}(\sigma_1 + \sigma_2 + \sigma_3) \quad \text{Equation 3}$$

$$q = \sqrt{\frac{1}{2}(\sigma_1 - \sigma_2)^2 + (\sigma_2 - \sigma_3)^2 + (\sigma_3 - \sigma_1)^2} \quad \text{Equation 4}$$

σ_1, σ_2 and σ_3 are the three principal stress. Equation 5 defines the relationship between failure strains as a fracture locus relative to stress triaxiality of conventional Ti-6Al-4V material which was first established by Giglio et al. (23) and later calibrated by Ullah et. al (24) for SLM Ti-6Al-4V manufactured lattice cells of similar diameter dimensions to the pints in the present work:

$$\varepsilon^{pl} = \begin{cases} \dfrac{D_1}{1+3\eta} + D_2 & -\dfrac{1}{3} < \eta \leq 0 \quad \text{Shear Failure} \\ D_3\eta + D_4\eta + D_5 & 0 < \eta \leq \eta_T \quad \text{Mixed Mode Failure} \\ D_6 + D_7 e^{(-D_6\eta)} & \eta_T \leq \eta \quad \text{Ductile Failure} \end{cases} \qquad \text{Equation 5}$$

In Equation 5, η_T is the transition point between mixed mode failure and ductile failure stress triaxility, and is indicated in the fracture locus shown in Figure 6a. The constants D_1 to D_7 of both conventional and SLM Ti-6Al-4V material are recorded in Table 4. Once the onset of damage is reached, the evolution of damage is characterised by the continuous exponential degradation of stiffness indicated by Equation 6.

$$D = \frac{1 - e^{-\alpha\left(\frac{u_{pl}}{u_{pl}^{f}}\right)}}{1 - e^{-\alpha}} \qquad \text{Equation 6}$$

In Equation 6, D is the damage variable used to define the degradation state of an element which is 0 when D is 1. The effective plastic failure displacement u_{pl} is defined by the multiplication of the total strain at failure (0.101) and typical element characteristic length of the titanium part. Plastic displacement at failure of 0.0018 mm and an exponent parameter of $\alpha = 2$ are able to capture the overall plastic deformation and failure of a tensile specimen accurately as shown in Figure 6b.

It is also assumed that the resin material exhibits a ductile failure mode, and the same calibrating process to determine the true plastic properties and damage process of resins is applied. Equation 7 defines the true plastic stress versus strain relationship. In addition, a similar stress triaxiality curve as for titanium is used for the resin material; however, the strain failure point of resin under tensile mode is now calibrated to be 0.85. This approach has the advantage that no predefined failure plane - as in the case of cohesive elements - needs to be defined to initiate material damage in the resin-rich zone. The stress versus strain curve is indicated in Figure 6 and is compared to the typical material property of bulk resins, which exhibit an elastic-plastic property with a total failure strain of approximately 0.38 in experimental data from (25):

$$\sigma_{pl} = 160\varepsilon_{pl}^{0.075} \qquad \text{Equation 7}$$

2.3.2. <u>Interface contact definition</u>

The interface between the resin and titanium parts was observed experimentally to follow an exponential decay law with increasing pin pull-out displacement. In this analysis, an exponential cohesive interaction law determined by the penalty stiffness K, maximum traction t, opening displacement δ and exponent α represents the interface. The traction value is 49 MPa, which was determined experimentally in previous work (8), while the damage evolution displacement δ is set equivalent to the pin length. The exponent α is calibrated to be 4.5, and a penalty stiffness of 10^6 MPa was used for all models. All details regarding the resin/titanium interface property C_2 (refer to Figure 5) are recorded in Table 5. The cohesive properties used to simulate spalling behaviour between elements in the resin rich zone C_1 (refer to Figure 5) are assumed to be equivalent to that of bulk epoxy resin. The strength of the material is taken from the study of Fard et al. (26), and the fracture toughness is taken from experimental study of Araki et al. (27) as indicated in Table 5.

3. RESULTS AND DISCUSSION

3.1. <u>Interface parameter calibration</u>

The cohesive interaction parameters are applied on the 0° pin of different sizes i.e. small (*L*=2.0, *D*=0.5) and large (*L*=3.5, *D*=1.0) pin, and the load versus displacement results are compared to the experimental data as shown in Figure 7a and Table 6. It is evident that the calibrated interface strength value of 49 MPa results in good agreement for the maximum load (within 9%) between FE and experimental data for both pin sizes. In addition, the exponential degradation law defined by the pin length and an exponent coefficient of α=4.5 accurately captures the deteriorating interface properties with increasing pull-out length seen in the experiments. In terms of pull-out energy, the predicted values are within 5% of the average experimental data for both cases (see Table 6). The close correlation indicates that the pull-out bridging law for both pin sizes can be predicted numerically with high precision under pure tensile loading. Subsequently, these laws can be used directly to determine the crack growth response of the joint in a DCB configuration with high accuracy using the multi-scale modelling procedure as presented in previous work (8, 9).

Using the calibrated cohesive parameters, a 20° pin model loaded at 0° is analysed with varying the friction coefficient from 0.1 to 0.9, and the results are indicated in Figure 7b and Table 6. It should be noted that the plotted Opening Traction Load is the global reaction load in the Z direction, which is at 20° with respect to the pin axis; while the Opening Displacement is the vertical displacement measured between the composite and the titanium component during the pull-out process. This is similar to the results obtained from the experimental test set-up. In general, Figure 7b indicates that the pull-out responses using friction coefficient values between 0.1 to 0.3 exhibit exponential decay with increasing pull-out length; while the response using the values between 0.5 to 0.9 show a more distinct two-part behaviour: (1) gradual decay and (2) plateau, which agrees better with what was seen in seen in experimental data. Furthermore, the values recorded in Table 6 show that the predicted maximum load agrees well with the experimental data for all friction coefficients (within 2%). However, the total pull-out energy is under-predicted by 14% with a friction coefficient value of 0.1 and is over-predicted by approximately 25% with values above 0.5. The values of 0.3 and 0.5 offer the closest correlation with the experimental pull-out energy (within 13%).

In terms of cavity damage post pull-out, it was found that numerical prediction of the 20° offset angle pin using a friction coefficient value of μ=0.5 correlate best with the CT scan cross-section of experimental specimens as indicated in Figure 8. The overall trend of resin crushing and spalling out is captured well. In particular, the area at the wedge made between the pin and the composite section that is completely spalled post pull-out is well predicted. Furthermore, the location at which the occurrence of spalling appears to be visible, which is two thirds of the pull-out length, also compared well between the numerical prediction and experimental result. The agreement with experimental data in terms of load response and damage mechanisms post pull-out indicates that the presented modelling scheme and calibrated interface parameters are effective at predicting the overall pull-out response of a single pin metal-composite hybrid joint for off-axis loading conditions. Therefore, the model can be reliably extended to study detailed pin behaviour under varying mode mix loading conditions to gain a more complete understanding of the pull-out process, which was not possible to observe and quantify in previous experimental work. The interaction exponential cohesive law and a friction coefficient value of $\mu=0.5$ are chosen for all analyses for the remainder of this study.

3.2. Analysis of offset angle pin

Figure 9 and Table 7 compare the pull-out load versus displacement response of the large pin ($L=3.5$, $D=1.0$) with a 10°, 20° and 30° offset angle between numerical prediction and experimental results. In general, the overall trend of pull-out response for all offset angle pin models is predicted with reasonable accuracy in terms of maximum load (4% difference in average), total pull-out energy (15% difference in average) and the increasing trends of these values with increasing mode mix loading ratio. Furthermore, while distinct two-part behaviour is shown in the pin pull-out response for the 20° and 30° pins, the 10° pin shows a more exponential decay, relatively, which is directly influenced by the pull-out damage.

Figure 10 shows the damage processes of the 20° offset angle pin model, and results are further correlated with the load response curve in Figure 9b as an example to illustrate the overall damage sequence occurring for pinned specimens under mode mix loading. Four distinct regions are observed when associating the element state and stresses with the load responses. In the first region, namely, the elastic slip region, the pin is pulled out with no permanent/visible interface damage as shown in Figure 10a. Following this, the pin pulls out progressively while bearing against the resin-rich region. Under continued pull-out, the pin further bears against the resin and the contact pressure stress between the pin and the resin continually increases (Figure 10b). This process produces crushing of the resin and plastic deformation of the pin. When the contact pressure reaches approximately 250 MPa, the resin is completely crushed and is spalled out to accommodate the pull-out process of the pin (Figure 10c). The plastic strain at which the elements within the resin-rich zone are deleted is approximately 0.8 (see Figure 8b). Once spalling occurs, the pin comes into contact with a new set of elements in the resin rich zone and the process is repeated with pin bending and resin crushing. This phenomenon correlates with the plateau region in the pull-out curve occurring at approximately 100 N and 1.75 mm pull-out length as shown in Figure 9c. Finally, the pin pull-out is complete when there is no longer any contact between the pin and the resin (see Figure 10d).

The damage process of the 10° and 30° model displays similar behaviour, and the damage area of the cavity becomes more prominent with increasing mixed mode loading. For the 10° pin model, only small amounts of spalling damage and pin bending occurred and thus no visible plateau region is observed for larger crack opening displacements as seen in Figure 9a. Evidently, the pin plastic strain of the 10° pin post pull-out is less compared to the 20° pin model (see Figure 11). Conversely, these damage mechanisms are more severe for the 30° pin as bearing stresses increase; this is reflected by higher loads for the plateau region indicated within the pull-out load versus displacement curve in Figure 9b. Furthermore, it should be noted that the pull-out energy of the 30° pin model is over-predicted by 29% when compared to the average experimental values. This is because, experimentally, the wedge region made between the pin and composite is spalled out by bearing pressure before the maximum shear strength of the interface is reached. This process was not captured numerically with the current modelling techniques and an extremely fine mesh is required to capture this phenomenon. Nevertheless, all aspects of the pull-out process are well predicted.

Furthermore, to validate the experimental test method of mimicking mode mix loading through the use of an offset angle pin, an analysis of 0° pin (D=1.0, L=3.5) loaded at 20° angle is compared with the 20° offset angle loaded at 0°. The results of both models compare well with each other and the experimental data in terms of load versus displacement response and damage process including progressive pin pull-out region, resin spalling and pin bending region with plateau loads. Further details about this validation process can be found in reference (28).

3.3. Effective aspect ratio for pull-out under mode mix loading

To gain full understanding on the effect of mode mix response on pin pull-out behaviour, the 0° pin with L/D aspect ratio of 3.5 was loaded under the full range of mode mixity ratio. The pull-out results are presented in Figure 12, and the respective failure mode is illustrated in Figure 13. For presentation purpose, only the results of mode mix range from 0.5 to 0.94 (30° - 70° loading angle) are presented in Figure 12 and Figure 13 to illustrate the differences in pin failure mode and energy absorption with increasing mode mixity (refer to Figure 9 for mode mix responses from 0 to 0.34).

In general, the pin is pulled out completely with increasing mode mix loading ratio from 0 to 0.64 with typical resin spalling and pin bending mechanisms (see Figure 13a). This pin pull-out behaviour is also reflected in the load response curve with typical two stage behaviour beyond the elastic slip as seen in Figure 12. Further increasing the mode mix ratio to 0.77, the pin pull-out continues to approximately half of the total pin length; however, once plastic deformation of the pin exceeds the pin strength, fracture occurs typically at the root of the pin (see Figure 13b). This pin fracture following pull-out behaviour is indicated by sudden load drops during the pull-out phase of the load responses. The pin pull-out length reduces to one third and one tenth of its length before fracture with increasing mode mix ratio 0.87 and 0.94, respectively (see Figure 13b and Figure 13c). No pull-out is seen for the 0.98 and 1.00 mode mix ratio.

The pull-out results in Figure 12 are further broken down into tensile (Z direction) and shear (Z direction) component, and the maximum load, pull-out energy as well as pin failure mode is summarised in Figure 14. The results indicate that the tensile component of the pull-out curve exhibits gradual reduction in failure energy while maintaining the same maximum load values with increasing mode mixity up to 0.64 or 40° loading angle. On the other hand, the shear component shows a linear increase and reaches its maximum at 0.64 mode mixity for both values. This is due to the fact that the pin is completely pulled-out (indicated in Figure 13a) and the bearing component becomes prominent in the pull-out process with increasing shear-dominated loading. Beyond this point, the shear load component continues to increase while tensile load and pull-out energy drops exponentially as the contact pressure between the pin and the composite exceeds the pin strength leading to pin fracture, which reduces energy absorption.

The pin failure mode is comprehensively mapped for variation in *L/D* aspect ratio and mode mixity ratio, and results are shown in Figure 15. The results indicate that when mode mixity is 0 (pure tension), a transition *L/D* aspect ratio value of 6 is predicted to achieve complete pin pull-out failure mode. Above this mode mix value, pin fracture failure mode occurs, and the pin fracture energy is reduced to approximately 30% of the energy with complete pin pull-out. This agrees well with the previous experimental data presented in reference. It is noted that the transition *L/D* ratio predicted numerically is higher than the value determined experimentally. This is because the experimentally tested small pin (*D*=0.5 mm) had inherent porosity distributed randomly along the pin, which reduced the pin strength from 1028 MPa to 725 MPa. As little porosity is seen for the large pin (*D*=1.0 mm), the material properties of the pin used in this numerical procedure were of the bulk material, hence higher predicted transition value.

The results in Figure 15 also indicate that when the pin *L/D* aspect ratio is below the critical value of 6, pin pull-out failure mode occurs for mode mixity loading ratio range from 0 to 0.5 (tensile-dominated loading). When the mode mixity is increased to 0.64 (shear-dominated loading), the critical value reduces to 3.5 for pin pull-out failure mode to occur, above this value, the pin is pulled out partially followed by pin fracture. The cross-pattern region in Figure 15 indicates this transition to pin failure. Further increasing the mode mixity to 0.98 (80° loading angle) sees gradual reduction in the critical aspect ratio value from *L/D*=3.5 to *L/D*=1.0. Under pure shear loading (90° loading angle), pin fracture modes are observed for all pin aspect ratios.

More broadly, the results indicated in Figure 15 also provide essential information on how the use of a different pin material under different loading condition affects the pin geometry. For a material with strength lower than titanium, e.g. aluminium, the pin transition aspect ratio under Mode I loading condition is reduced as the pin strength is directly proportional to the *L/D* value. Furthermore, the transition *L/D* curve under mode mix loading will shift such that complete pull-out mode occurs at a lower mode mixity ratio due to lower ductility and bearing strength to sustain pin bending effect. On the other hand, a material with higher ductility such as stainless steel is more likely to achieve complete pull-out mode under a higher mode mixity ratio due to improved resistance to fracture during pin bending. Finally, the results indicate that the pin must be relatively thick and short to absorb high strain energy under shear-dominated loading.

4. CONCLUSION

A numerical investigation was carried out in this study to quantify the pin critical length/diameter aspect ratio to achieve pin pull-out failure mode under the full range of mode mixity loading ratio. A modelling methodology was first developed taking into account important aspects of the composite microstructure and incorporating the corresponding damage models for each respective materials and interfaces. The pin/composite interface is simulated with two interaction properties: (1) exponential interface cohesive law and (2) global Coulomb friction/pressure contact. The developed cohesive laws predicted well the pull-out response of small pin (L=2.0, D=0.5) and a large pin (L=3.5, D=1.0) specimens under pure Mode I (tensile) loading. When shear loading component is introduced, a friction coefficient of μ=0.5 was found to provide closest comparison with the relevant experimental data. Correlating the damage profile with load response during the pull-out process of the offset angle pins shows four distinct regions: (1) elastic slip; (2) progressive pull-out with gradual reduction in load; (3) resin spalling and pin bending with plateau loads; (4) loss of contact and sudden reduction in load. Increasing the mode mixity ratio, the resin spalling damage is more prominent as the bearing component increases. This behaviour agrees well with experimental observations.

Parametric investigation on the effect of pin geometry on pull-out failure mode under a full range of mode mix loading effectively indicated three sections in the map of L/D aspect ratio versus mode mix loading ratio: (1) pin fracture; (2) complete pin pull-out and (3) pin pull-out followed by pin fracture. The pin fracture section is defined by the area above an L/D aspect ratio of 6, below which, the pin is pulled-out for all tensile dominated loading (mode mixity range 0 to 0.5). The energy of the pin fracture mode is approximately 30% of the total pin pull-out failure mode. Once the loading condition is shear dominated, the critical aspect ratio reduces to 4.5 and 1.0 for 0.64 and 0.98 mode mixity ratio, respectively, to ensure pull-out occurs. When the aspect ratio is higher than the critical value under mode mix loading, the pin initially pulls out and then fractures due to the additional bending stresses acting. The total energy absorption of this failure mode is between 31% and 99% of the complete pin pull-out energy. These results indicated that the pin should be designed as relatively thick and short to pull out completely for high fracture energy under shear-dominated loading. Furthermore, together with the models at structural scale level and the multi-scale modelling methodology developed in previous publications [8, 9], this high precision numerical model completes the numerical procedure needed for analysis and optimization of a pin-reinforced hybrid joint

ACKNOWLEDGEMENTS

The authors acknowledge the efforts of Mr Aaron Pateras for manufacturing of SLM structures, Mr Robert Ryan for support during composite lay-up and curing, and Mr Peter Tkatchyk and Mr Julian Bradler for providing assistance during mechanical testing. One of the authors, A.T.T. Nguyen acknowledges financial support through a RMIT PhD International

Scholarship (RPIS). One of the authors, S. Feih, acknowledges the support from the Agency for Science, Technology and Research (A*STAR) and the Science and Engineering Research Council (SERC) of Singapore through the Additive Manufacturing Centre Initiative (SERC Grant No. 142 68 00088).

REFERENCES

1. Graham D.P. RA, Baker D., Smith P.A, Watts J.F. A Hybrid Joining Scheme For High Strength Multi-Material Joints. Proceedings of 18th International Conference on Composite Materials; South Korea2011.

2. Tu W, Wen PH, Hogg PJ, Guild FJ. Optimisation of the protrusion geometry in Comeld™ joints. Composites Science and Technology. 2011;71(6):868-76.

3. Ucsnik S, Scheerer M, Zaremba S, Pahr DH. Experimental investigation of a novel hybrid metal–composite joining technology. Composites Part A: Applied Science and Manufacturing. 2010;41(3):369-74.

4. Heimbs S, Nogueira AC, Hombergsmeier E, May M, Wolfrum J. Failure behaviour of composite T-joints with novel metallic arrow-pin reinforcement. Composite Structures. 2014;110(0):16-28.

5. Philip NP, Richard B, Darryl A. Growth of Damage in Additively Manufactured Metal-Composite Joints. Proceedings of 15th European Conference on Composite Materials; Venice Italy2012.

6. Philip NP, Richard B, Darryl A. Fatigue of Metal-Composite Joints with Penetrative Reinforcement. 54th AIAA/ASME/ASCE/AHS/ASC Structures, Structural Dynamics, and Materials Conference. Structures, Structural Dynamics, and Materials and Co-located Conferences: American Institute of Aeronautics and Astronautics; 2013.

7. Kashaev N, Ventzke V, Riekehr S, Dorn F, Horstmann M. Assessment of alternative joining techniques for Ti–6Al–4V/CFRP hybrid joints regarding tensile and fatigue strength. Materials & Design. 2015;81:73-81.

8. Nguyen ATT, Brandt M, Orifici AC, Feih S. Pin pull-out behaviour for hybrid metal-composite joints with integrated reinforcements. Composite Structures. 2016;93(11):2685-95.

9. Nguyen ATT, Amarasinghe CK, Brandt M, Feih S, Orifici AC. Loading, support and geometry effects for pin-reinforced hybrid metal-composite joints. Composites Part A: Applied Science and Manufacturing. 2017;98:192-206.

10. Bianchi F, Zhang X. A cohesive zone model for predicting delamination suppression in z-pinned laminates. Composites Science and Technology. 2011;71(16):1898-907.

11. Bianchi F, Zhang X. Predicting mode-II delamination suppression in z-pinned laminates. Composites Science and Technology. 2012;72(8):924-32.

12. Zhang B, Allegri G, Hallett SR, editors. High-fidelity fe modelling of Z-pins in quasi-isotropic laminates. 16th European Conference on Composite Materials, ECCM 2014; 2014.

13. Cui H, Li Y, Koussios S, Beukers A. Mixed mode cohesive law for Z-pinned composite analyses. Computational Materials Science. 2013;75(0):60-8.

14. Cui H, Li Y, Koussios S, Zu L, Beukers A. Bridging micromechanisms of Z-pin in mixed mode delamination. Composite Structures. 2011;93(11):2685-95.

15. Meo M, Achard F, Grassi M. Finite element modelling of bridging micro-mechanics in through-thickness reinforced composite laminates. Composite Structures. 2005;71(3–4):383-7.

16. Li C, Wu Z, Meng Z, Li M. Influential Factors of Z-pin Bridging Force. Applied Composite Materials. 2014;21(4):615-31.

17. Sweeting RD, Thomson RS. The effect of thermal mismatch on Z-pinned laminated composite structures. Composite Structures. 2004;66(1–4):189-95.

18. Nguyen ATT, Brandt M, Orifici AC, Feih S. Hierarchical surface features for improved bonding and fracture toughness of metal–metal and metal–composite bonded joints. International Journal of Adhesion and Adhesives. 2016;66:81-92.

19. Group AC. ACG VTM 260 Series2006. Available from: http://www.lavender-ce.com/wp-content/uploads/pds1154-vtm260-issue5.pdf.

20. Brandt M, Sun S, Leary M, Feih S, Elambasseril J, Liu Q. High-value SLM aerospace components: From design to manufacture. Advanced Materials Research. 2013;633:135-47.

21. ABAQUS Version 6.8 Documentation Collection 2010 [updated April 20th.

22. Bai Y, Wierzbicki T. A new model of metal plasticity and fracture with pressure and Lode dependence. International Journal of Plasticity. 2008;24(6):1071-96.

23. Giglio M MA, Vigano F. Ductile fracture locus of Ti-6AL-4V titanium alloy. International Journal of Mechanical Sciences. 2012;54:121-35.

24. Inam Ullah MB, Stefanie Fieh. Performance of bio-inspired Kagome truss core structures under compression and shear loading. COMPOSITE STRUCTURE. 2014;118:294-302.

25. Measurement of Epoxy Resin Tension, Compression, and Shear Stress–Strain Curves over a Wide Range of Strain Rates Using Small Test Specimens. Journal of Aerospace Engineering. 2008;21(3).

26. Fard M, Liu Y, Chattopadhyay A. Characterization of Epoxy Resin Including Strain Rate Effects Using Digital Image Correlation System. Journal of Aerospace Engineering. 2011;25(2):308-19.

27. Araki W, Nemoto K, Adachi T, Yamaji A. Fracture toughness for mixed mode I/II of epoxy resin. Acta Materialia. 2005;53(3):869-75.

28. Nguyen ATT. Nature-inspired aerospace hybrid structural joint concepts realised by additive manufacturing. Melbourne: RMIT University; 2017.

Table 1: Numerical analysis matrix

Analysis Type	*L* [mm]	*D* [mm]	(Φ) [Degree]	Calibration parameters	Output
Calibration	3.5	1.00	0	Cohesive exponential law	
	2.0	0.50	0	Cohesive exponential law	
	3.5	1.00	20	Contact Friction Coefficient	
Geometrical behaviour	3.5	1.00	10	--	Load versus displacement response
	3.5	1.00	30	--	Pull-out process and damage behaviour
Mode mix loading	0.5 - 6.5	1.0	0 - 90	--	Mode mix loading response
				--	Aspect ratio spectrum Failure mode map

Table 2: Fibre waviness region parameters

Pin orientation	Φ (°)	H_1 / D_h	H_2 / D_h	V_1 / D_v	V_2 / D_v
Along fibres	0	2.9	3.0	3.1	3.0
	10	2.2	2.8	2.9	3.0
	20	2.4	3.0	3.1	3.0
	30	2.3	2.9	3.0	3.0

Table 3: Material properties of VTM264[19] , epoxy resin and Ti-6Al-4V [20]

VTM264		VTM264		Epoxy Resin		Ti-6Al-4V	
E_{11} (MPa)	120000	X_T (MPa)	2459	E (MPa)	3900	E (MPa)	110000
E_{22} (MPa)	7500	X_C (MPa)	1150	v	0.37	G (MPa)	42500
E_{33} (MPa)	7500	Y_T (MPa)	45	σ_y (MPa)	80	v	0.32
G_{12} (MPa)	3900	Y_C (MPa)	200			σ_y (MPA)	1070
G_{13} (MPa)	3900	S_{12} (MPa)	85				
G_{23} (MPa)	2300	S_{13} (MPa)	85				
v_{12}	0.32	S_{23} (MPa)	85				
t_{ply} (mm)	0.21	G_{ft} (kJ/m^2)	100				
		G_{fc} (kJ/m^2)	25				
		G_{mt} (kJ/m^2)	0.46				
		G_{mc} (kJ/m^2)	1.6				

Table 4: Constant used to define relationship between failure strain and stress triaxiality

Constants	D_1	D_2	D_3	D_4	D_5	D_6	D_7	η_T
Ti-6AL-4V Billet (23)	0.164	0.292	1.376	-0.052	0.461	1.89	1.853	0.49
Ti-6AL-4V SLM (24)	0.1	0.1	1.3	-0.03	0.2	1.15	2.0	0.458

Table 5: Cohesive contact parameters used for resin/titanium and resin/resin interfaces

Cohesive parameters	Interface Interaction Pair	
	Resin/titanium (C_2)	Resin/resin (C_1)
Strength $\boldsymbol{t_n}$ (MPa)	49[(1)]	80[(3)]
Strength $\boldsymbol{t_s}$ (MPa)	49[(1)]	80[(3)]
Fracture toughness $\boldsymbol{G_{IC}}$ (J/m^2)	-	1.1[(3)]
Fracture toughness $\boldsymbol{G_{IIC}}$ (J/m^2)	-	1.5[(3)]
Damage Evolution Displacement $\boldsymbol{\delta}$ (mm)	Pin length	-
Exponential alpha $\boldsymbol{\alpha}$	4.5[(2)]	-
Penalty Stiffness K_n (MPa)	1,000,000[(3)]	1,000,000[(3)]
Power law coefficient η	1.21[(3)]	1.21[(3)]

(1) Calculated from experimental data; (2) Calibrated to fit with experimental data; (3) based on literature data[(31)]

Table 6: Pull-out results of 0° and 20° offset angle pin with calibrated cohesive interaction law and friction coefficient.

L [mm]	*D* [mm]	(Φ) [Degree]	μ	Max load (N)			Pull-out Energy (J)		
				EXP	FE	EXP, FE % Difference	EXP	FE	EXP, FE % Difference
2	0.5	0	--	189	196	4%	100	98	-2%
3.5	1	0	--	567	620	9%	433	453	5%
3.5	1	20	0.1	641	630	-2%	616	532	-14%
3.5	1	20	0.3	641	630	-2%	616	642	4%
3.5	1	20	0.5	641	630	-2%	616	693	13%
3.5	1	20	0.7	641	630	-2%	616	765	24%
3.5	1	20	0.9	641	630	-2%	616	777	26%

Table 7: Comparison of experimental and FE predicted pull-out results of offset angle pins

L [mm]	*D* [mm]	(Φ) [Degree]	μ	Max load (N)			Pull-out Energy (J)		
				EXP	FE	EXP, FE % Difference	EXP	FE	EXP, FE % Difference
3.5	1	10	0.5	663	624	-6%	578	562	-3%
3.5	1	20	0.5	641	630	-2%	616	693	13%
3.5	1	30	0.5	607	637	5%	568	734	29%

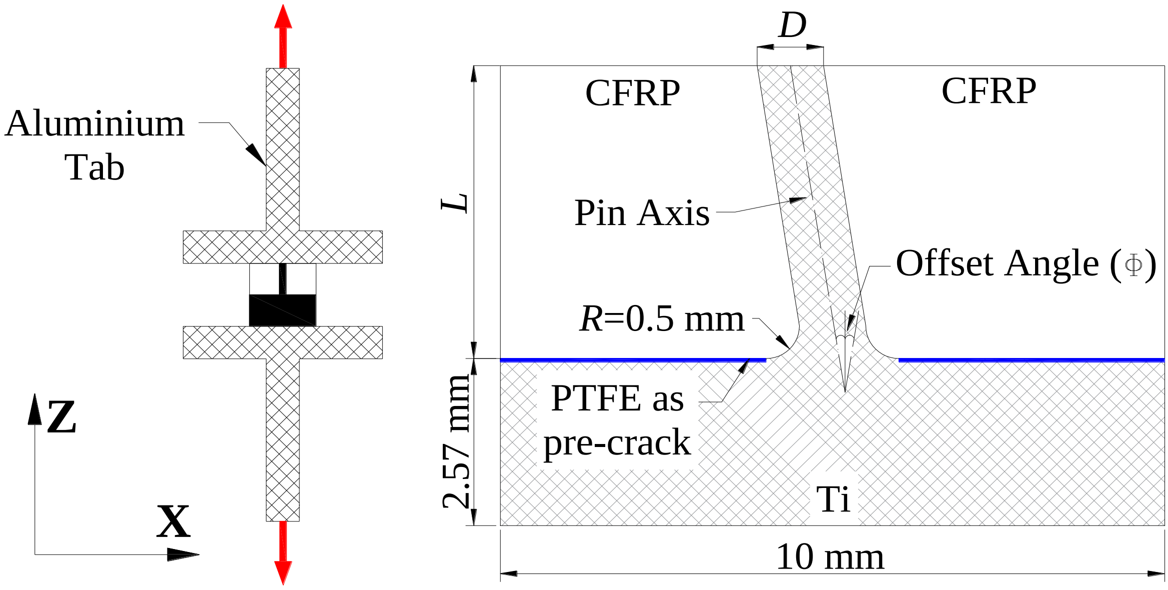

Figure 1: Pull-out test setup of a single pin specimen with detail cross-section schematic

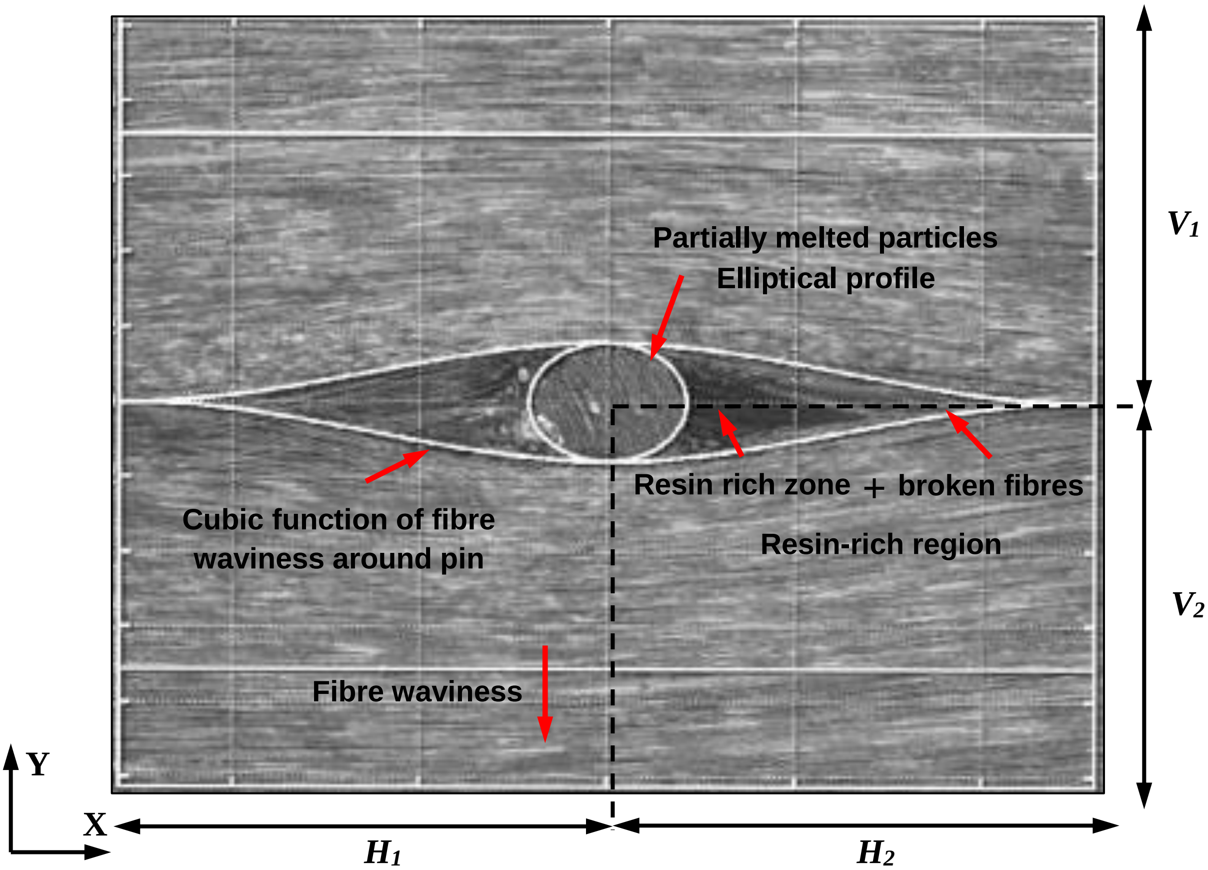

Figure 2: Typical in-plane cross-section of a pull-out specimen with modelling geometrical assumptions

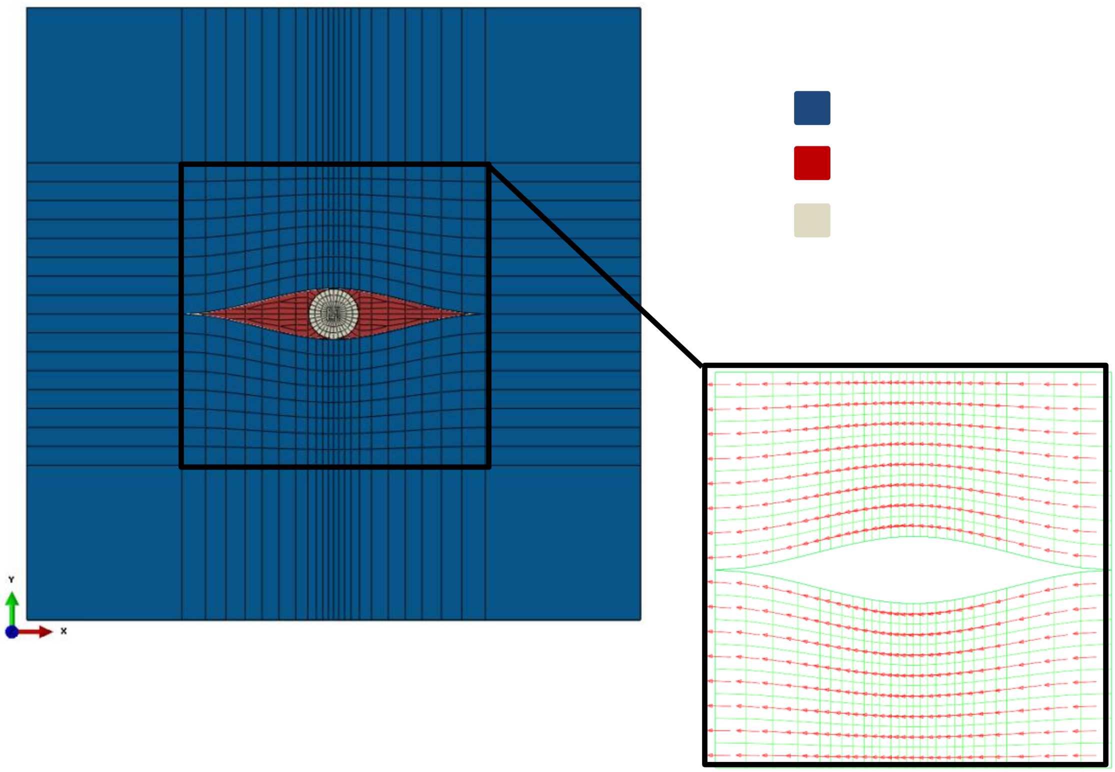

<u>Figure 3</u>: In-plane cross-sectional meshing scheme with composite fibre orientation

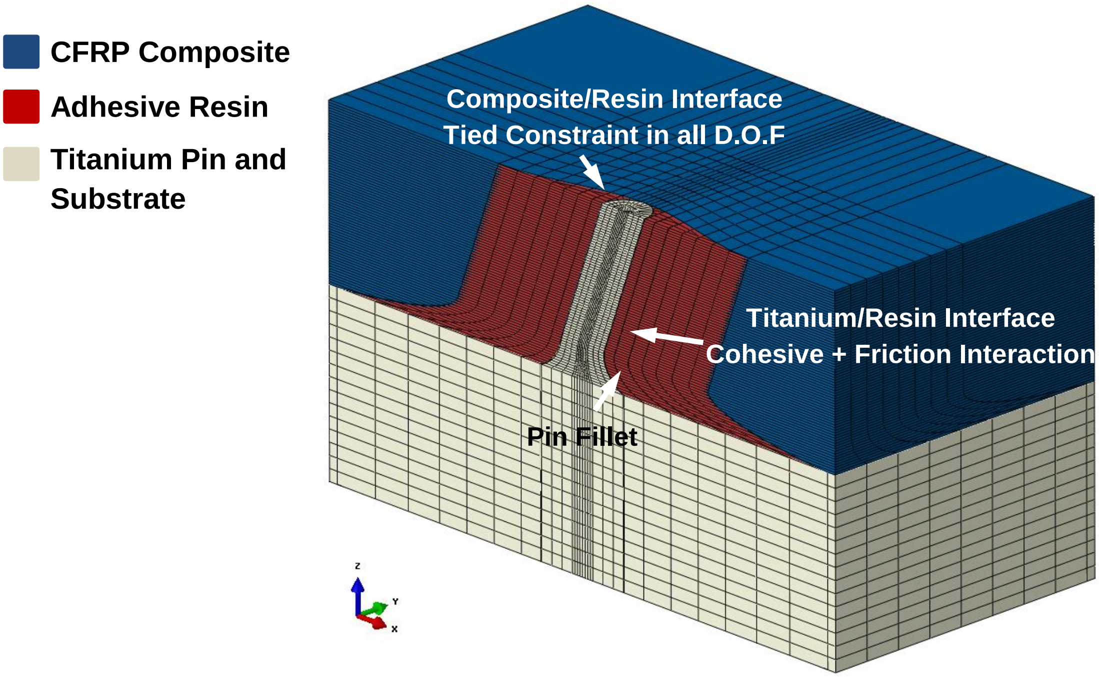

Figure 4: Through-thickness cross-sectional meshing scheme indicating tied constraints between composite/resin and cohesive and friction interaction at titanium/resin

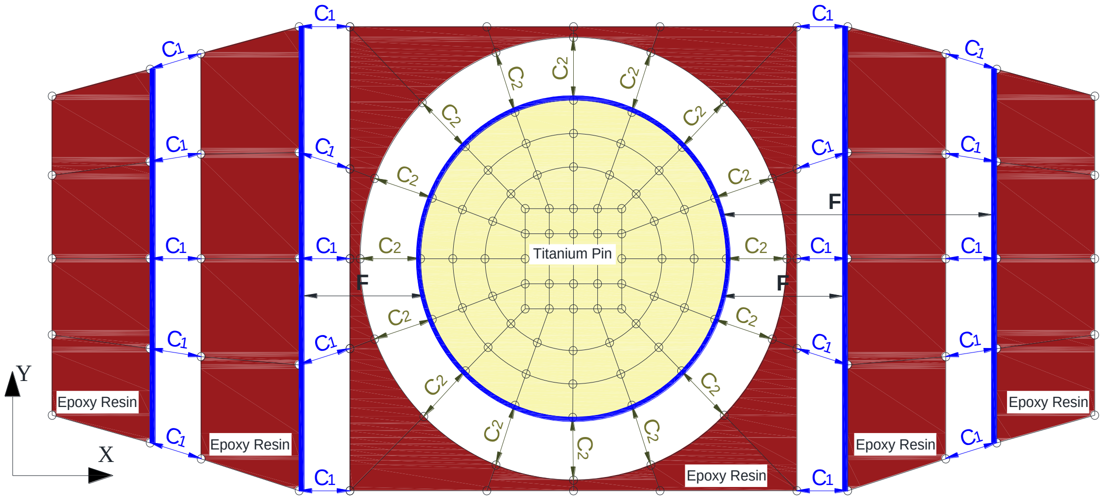

Figure 5: Modelling methodology showing contact definition at the titanium/resin and resin/resin interface with C: Cohesive Contact and F: Coulomb Friction Contact

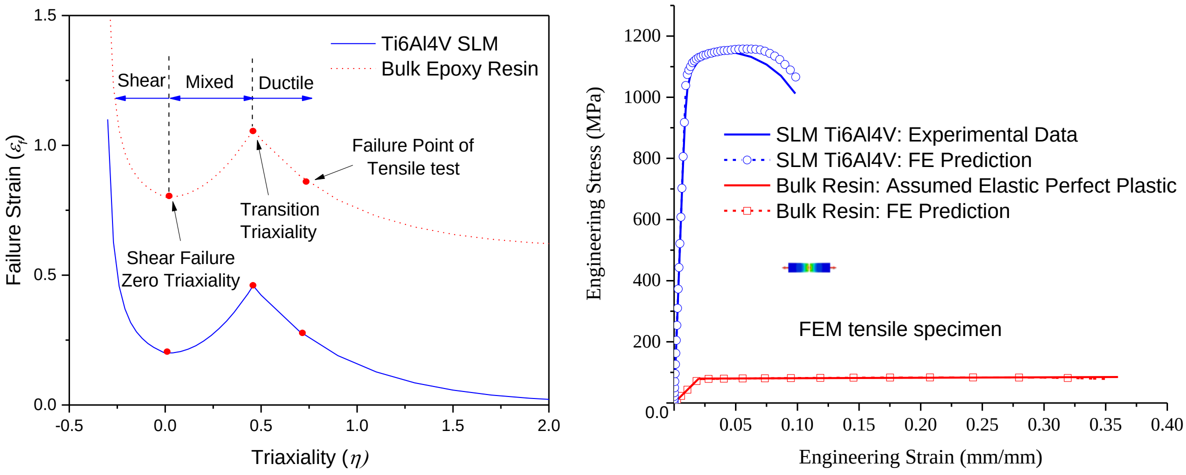

(a) *(b)*

Figure 6: (a) Failure strain for Ti-6AL-4V and epoxy resin with varying stress triaxiality; (b) correlation between FE and experimental data [24]

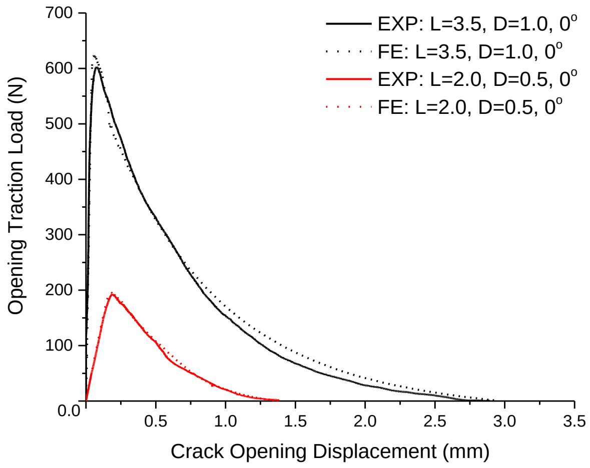

(a)

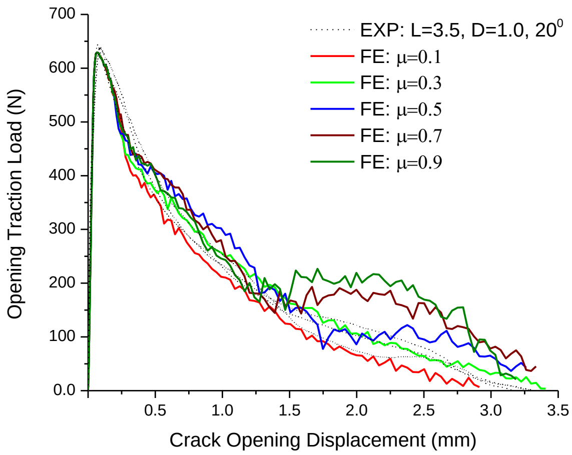

(b)

Figure 7: Parameter calibration for (a) interface cohesive interaction law of the 0° pin and; (b) friction coefficient for bearing effect of the 20° pin

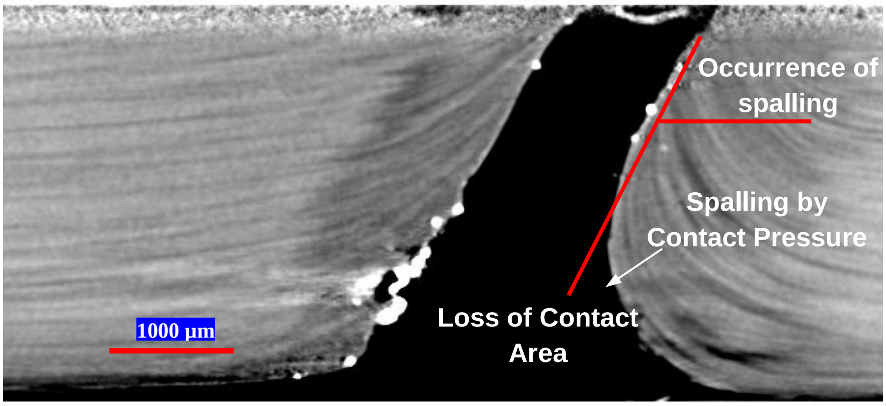

(a)

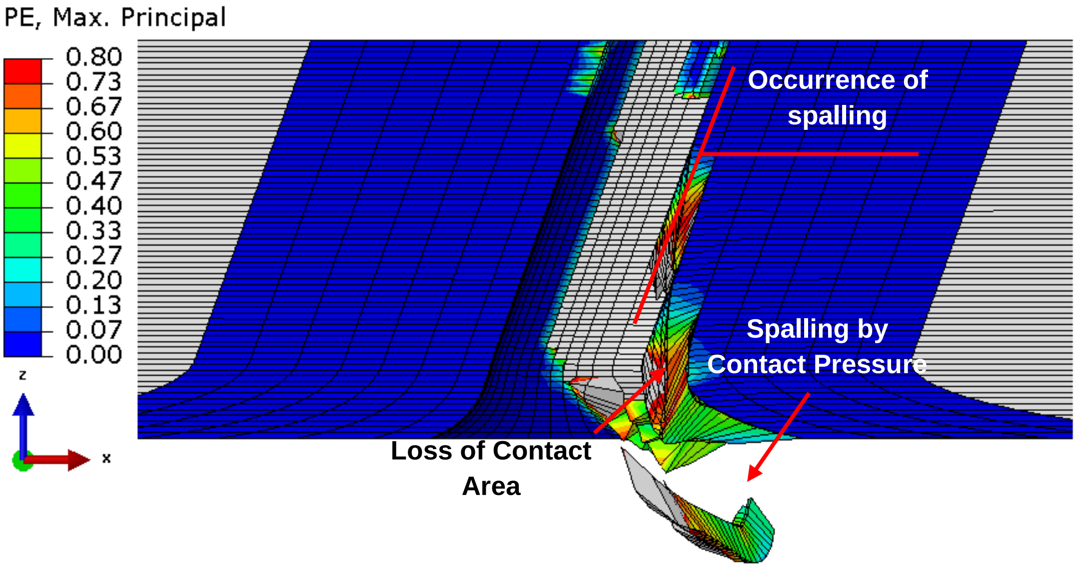

(b)

<u>Figure 8</u>: Pin cavity cross-section post pull-out of the 20° pin (a) CT scan and (b) FE analysis showing resin plastic strain and spalling phenomenon

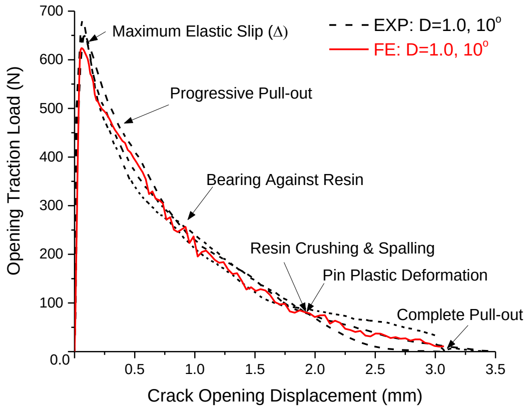

(a)

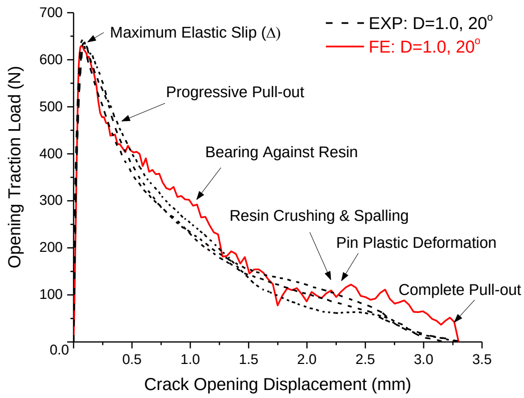

(b)

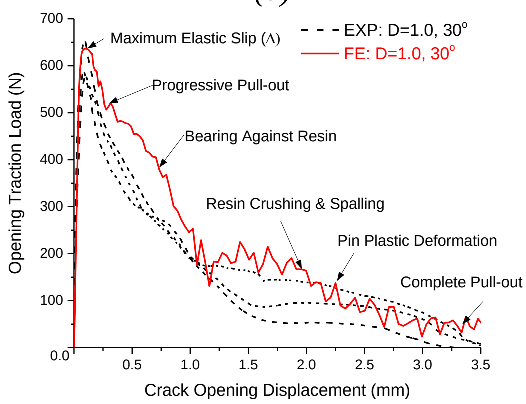

(c)

Figure 9: Pull-out response comparison of offset angle pins between experimental data (dotted lines) and numerical results (solid lines) using 0.5 friction coefficient for (a) 10° pin; (b) 20° pin and (c) 30° pin showing damage processes

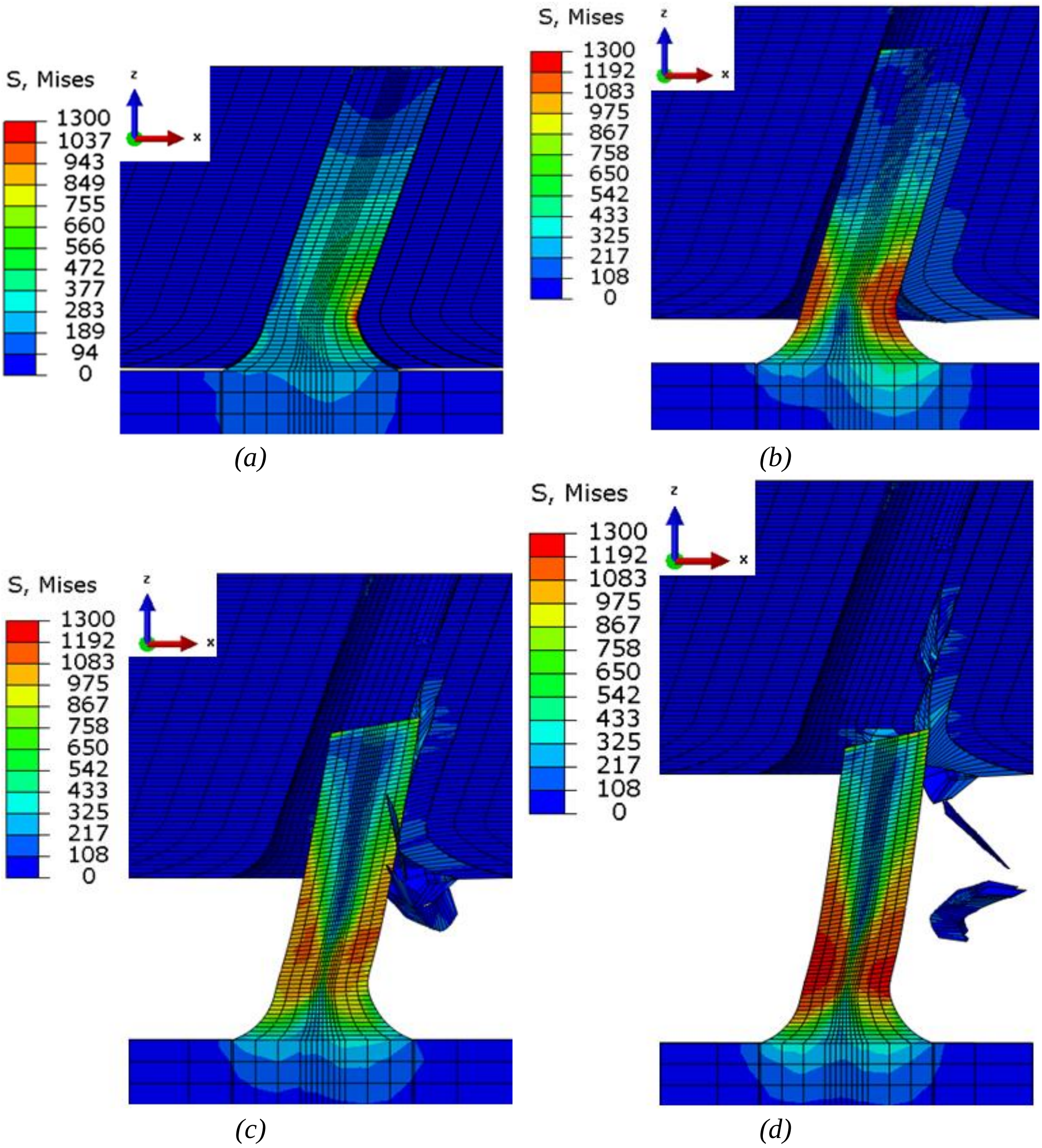

Figure 10: Von Mises stress (in MPa), showing damage mechanisms throughout the pin pull-out process (a) Elastic Slip; (b) Pull-out and bearing against resin; (c) Resin spalling and pin bending; (d) Complete pull-out

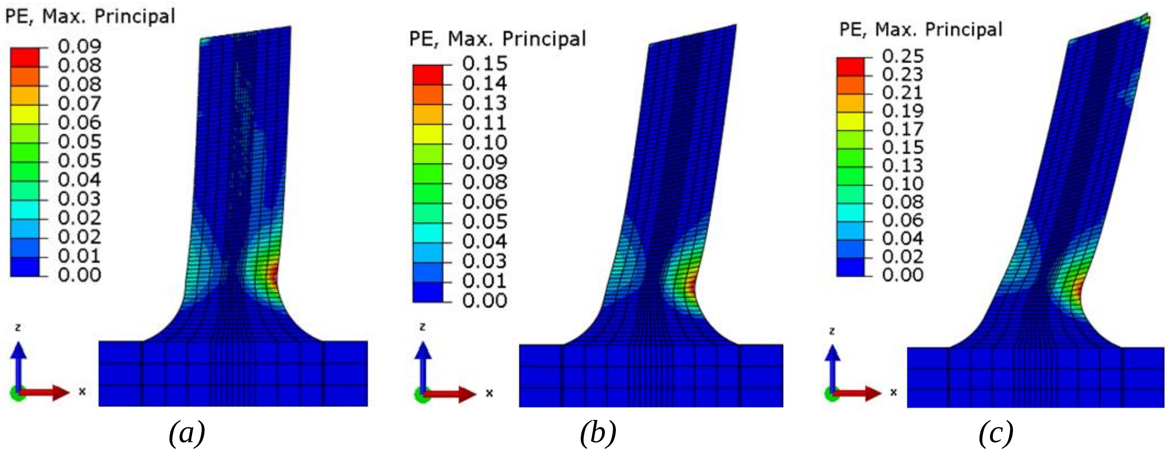

Figure 11: Plastic strain at complete pull-out of offset angle pin; (a) 10°; (b) 20° and (c) 30°

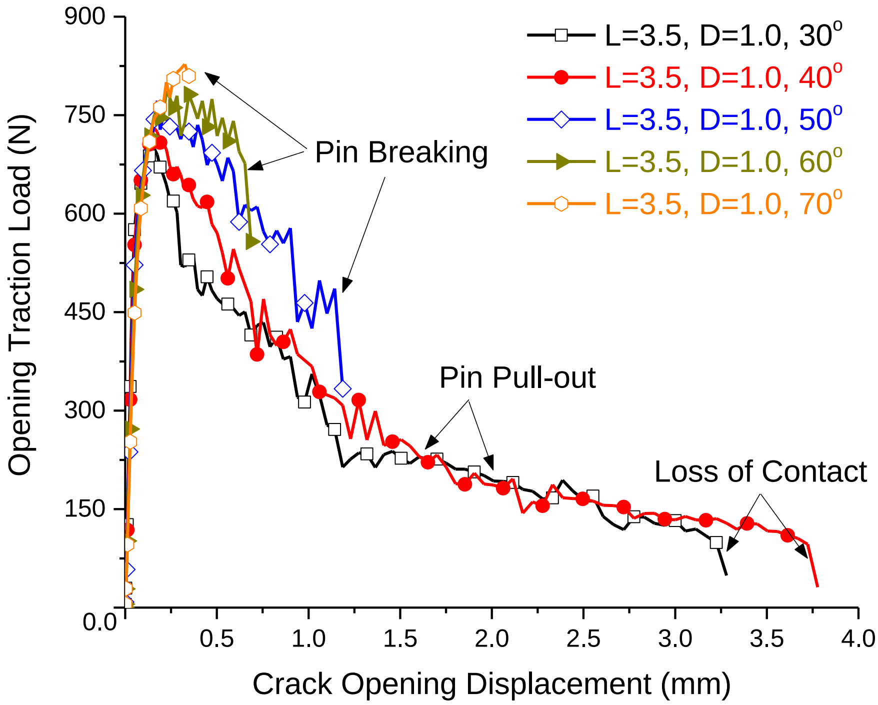

Figure 12: Pull-out response of 0° pin under mode mix loading

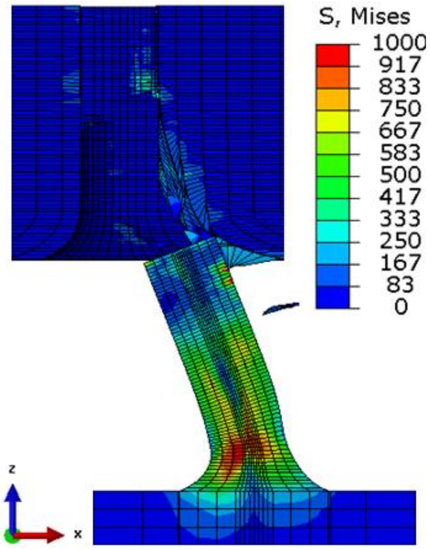

(a)

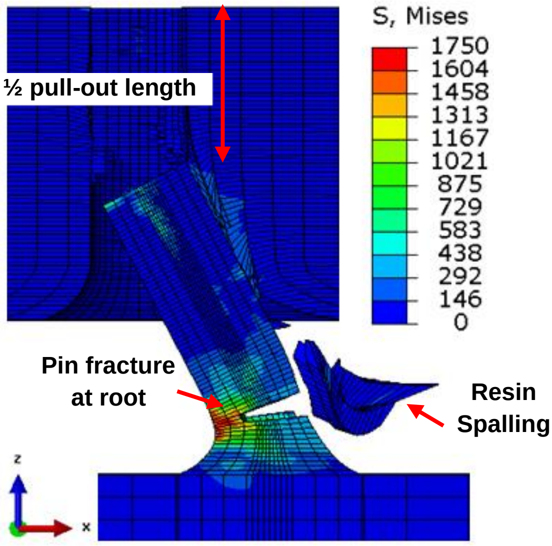

(b)

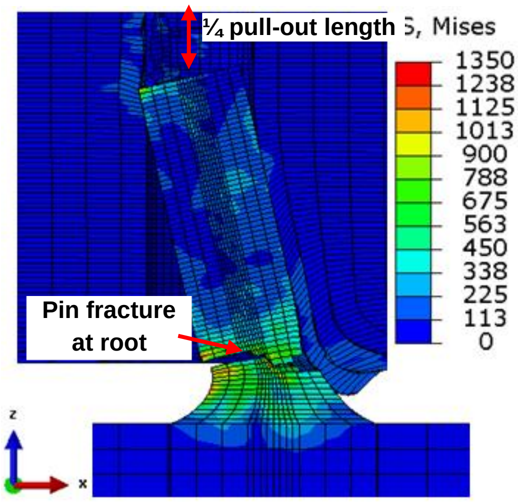

(c)

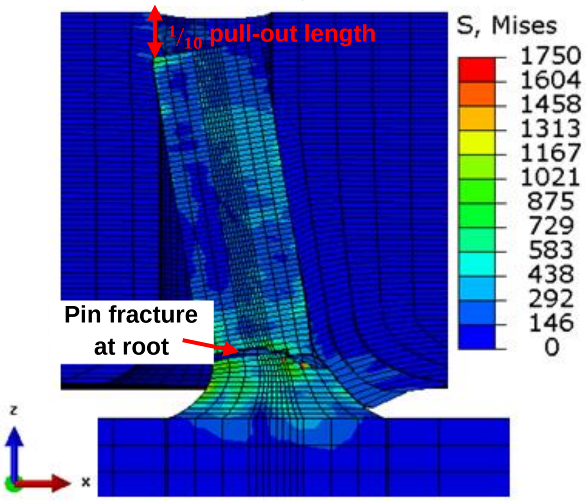

(d)

Figure 13: Von Mises stress in MPa showing pull-out damage modes of pins under mode mix loading at (a) 40°; (b) 50°; (c) 60° and (d) 70°

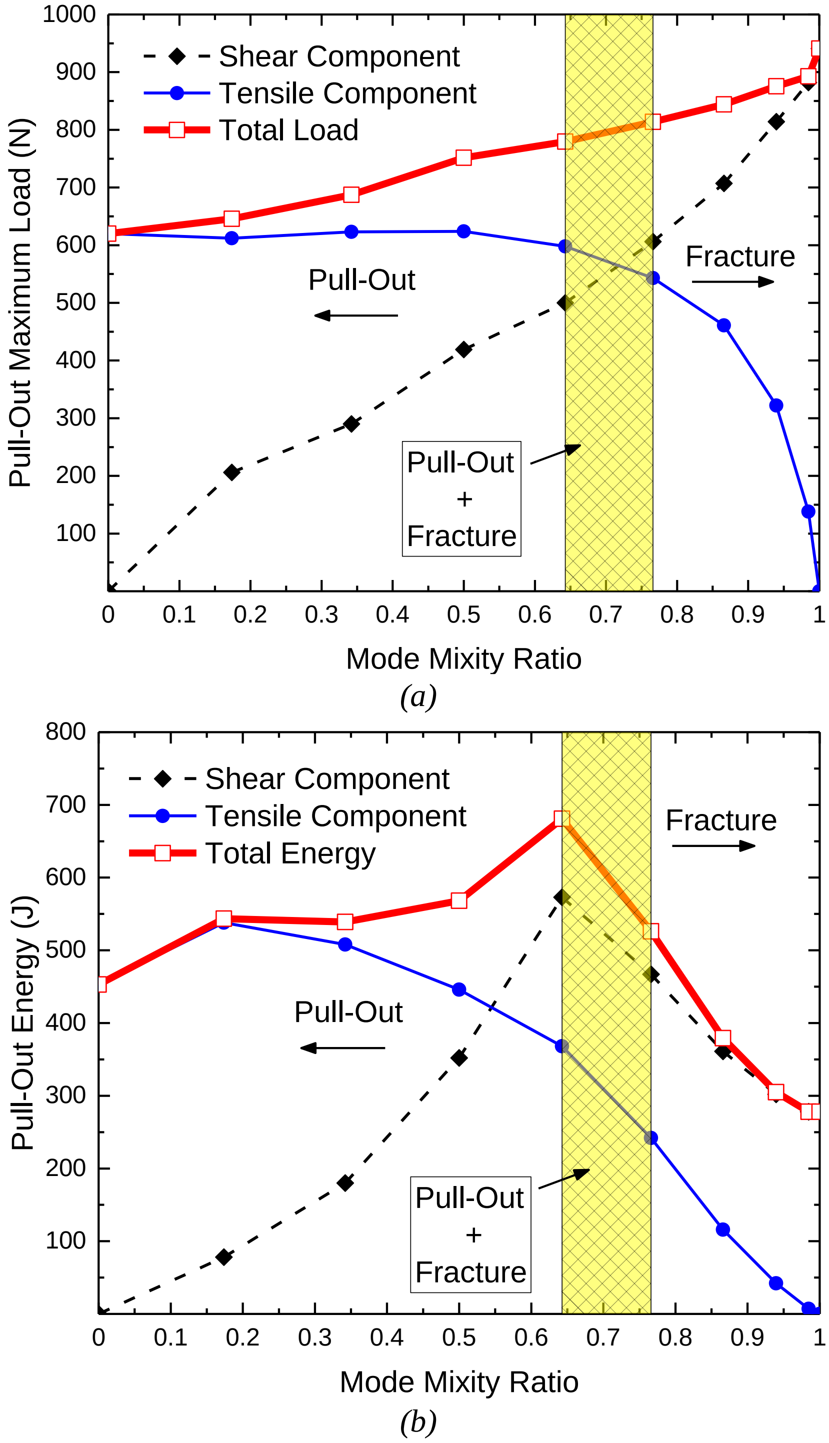

Figure 14: (a) Maximum pull-out load and (b) total pull-out energy versus mode mixity ratio with failure mode indicated

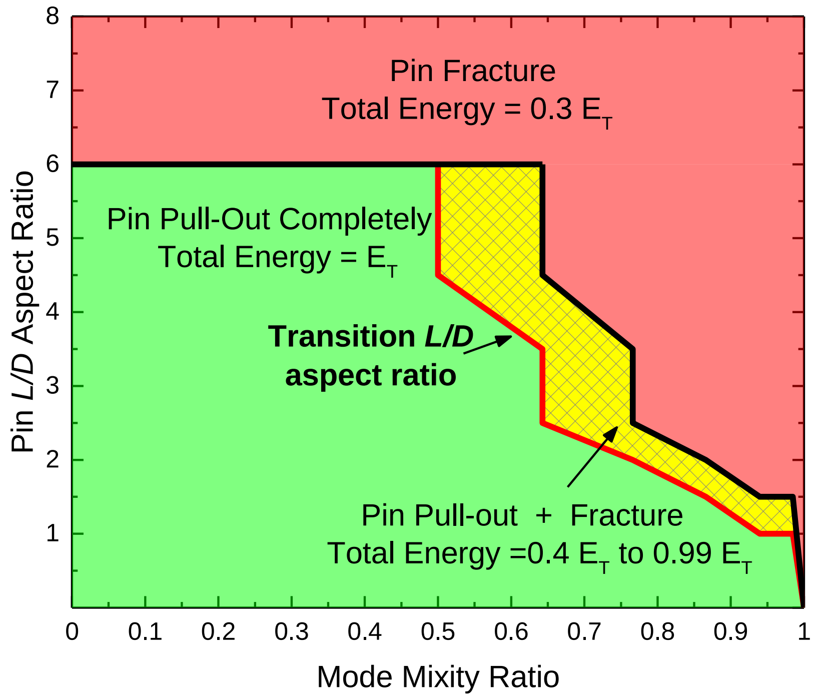

Figure 15: Failure mode for varying L/D aspect ratio and mixed mode angle